Overtopping breaching of river levees constructed with cohesive sediments

H. Y. Wei[1], M. H. Yu[1], D. W. Wang[2], Y.T. Li[1]

[1]State Key Laboratory of Water Resources and Hydropower Engineering Science, Wuhan University, Wuhan, 430072, People's Republic of China

[2]State Key Laboratory of Simulation and Regulation of River Basin Water Cycle, China Institute of Water Resources and Hydropower Research, Beijing, 100038, People's Republic of China

Correspondence to: M. H. Yu (mhyu@whu.edu.cn)

Abstract. Experiments were conducted in a bend flume to study the overtopping breaching process and the corresponding overflow rate of river levees constructed with cohesive sediments. The river and land regions were separated by the constructed levee model in the bend flume. Results showed that the levee breaching process can be subdivided into a slope erosion stage, a headcut retreat stage and a breach widening stage. Mechanisms such as scour-hole erosion, flow shear erosion, impinging jet erosion, side slope erosion and cantilever collapse were discovered in the breaching process. The erosion characteristics were determined by both flow and soil properties. Finally, the levee breaching flow rates were simulated by a depth averaged 2-D flow model. The calculated overflow rates can be well expressed by the broad-crested weir flow formula. The deduced discharge coefficient was smaller than that of common broad-crested rectangular weirs because of the shape and roughness of the breach.

1 Introduction

River levees, as a kind of embankment structure, are constructed around rivers and parallel to the main flow to constrain flow and protect local residents from flooding disasters (Schmocker and Hager, 2009). Levees constructed with cohesive sediment are the most common type due to their low cost and the convenience with which construction materials can be acquired locally. When lacking a protection layer, this kind of levees can be easily breached by overtopping flow if water level exceeds the design water level including the freeboard (Pickert et al., 2011). Consequently, the protected area will be submerged, threatening lives and properties. Under the circumstances, predicting flood propagation processes and repairing the levee breach as soon as possible is crucial for diminishing losses. For this, a profound understanding of cohesive levee breaching process and overflow rates is necessary.

Many researches have been performed on the overtopping breaching of embankments constructed normal to river flow and quite a few of these are for embankments constructed with non-cohesive materials. For example, Coleman et al. (2004) found that the breach channel of overtopped embankments under constant water level has a curved shape and the breach development obeyed the minimum energy dissipation rate rule for streams. Schmocker and Hager (2009) studied the limitations on sediment size, dike width, dike height and unit discharge in laboratory experiments of non-cohesive dike breach. Pontillo et al. (2010) applied a one-dimensional two-phase model to simulate flow propagation and breaching process of a trapezoidal-shaped sediment dike, and the results were proved to be reasonable. Pickert et al. (2011) found that embankments composed of finer materials exhibited discontinuous erosion affected by cohesion due to pore-water pressure. Based on large amount of experiment data, Schmocker and Hager (2012) proposed some normalized formulae including dimensionless equilibrium dike height, equilibrium dike volume and maximum breach discharge versus approach flow discharge, initial dike height and sediment diameter.

Many studies on the cohesive ones have also been conducted. Compared to non-cohesive embankments, overtopping breaching of cohesive embankments is a more complex phenomenon involving impinging jet flows, reverse roller structures and headcut erosion (Zhu, 2006). Many researchers(Ralston, 1987; Powledge et al., 1989; Hanson et al., 1999; Wahl, 2004) have found that headcut retreat is a predominant mode during the overtopping breaching process of cohesive embankments and many prediction models of headcut retreat rate were put forward (Hanson et al., 2001; Stein and LaTray, 2002; Zhao et al., 2013). Zhu (2006) developed a model for overtopping breaching of cohesive embankments in which the headcut erosion process was included. Hanson (1999), Zhu (2011) and the IMPACT project (Morris et al., 2005) all studied the cohesive embankment breach process based on laboratory experiments and large-scale experiments. And the latter two were also concerned with the influence of soil properties, embankment geometry and so on. Both the IMPACT project (Morris et al., 2005) and Zhang et al. (2009) conducted a series of experiments on cohesive dam break. And Zhang et al. (2009) also studied the cause of headcut erosion, double spiral flow at the dam crest and the effect of soil cohesion on breach process.

However, researches on the overtopping breaching of river levees parallel to the main flow are limited. Kakinuma and Shimizu (2014) conducted large-scale experiments on breaching of non-cohesive river levees at the floodway of an actual river channel. The breach development was categorized into four stages according to breach progress and hydraulic characteristics. Yu et al. (2013) studied the influencing factors on the overtopping breaching process of non-cohesive levees and the breach discharge properties. Liang et al. (2002) built a numerical model to simulate The Yellow River dike breach. The levee materials were a combination of non-cohesive and cohesive soils. The riverbank widening model proposed by Osman and Thorne (1998) was adopted in calculating the breach enlargement.

River levee breach is quite different from the breach of embankment constructed normal to the flow in morphology, hydraulics and inflow variation characteristics (Kakinuma and Shimizu, 2014). Moreover, measured data of cohesive levee breach have not been reported until now. Hence, four groups of experiments on cohesive levee breach were performed in a bend flume with varied inflow discharge, soil water content and porosity. In these experiments, levees were constructed in the flume with an initial breach. Different stages of levee breach process and flow characteristics near the breach were analyzed. The levee breaching flow rates process, simulated by a depth averaged 2-D flow model, was also studied with detail.

2 Experiment setup

Due to the combined action of gravity and centrifugal force on bend flow, the water surface at the concave bank is higher than that at the convex bank. So levees at the concave bank are more likely to be breached by overflow than that at convex bank or straight channels. So, to simulate this kind of more frequent levee breach, we conduct the experiments in a bend flume with the plane shape of "U" and bed slope of about 1/1000. Fig. 1a shows the experiment layout. The levee was built from the bend apex to the exit of the flume and the cross-section of the levee is shown in Fig. 1d. Initially, flow was restrained by the levee and a dry area at the outer side of the levee was separated from the wet part. The dry area, which will be submerged after the levee breaching, is named as the land region. While the remaining wet reach is the river region. The initial breach was located at the place where overtopping breaching is most likely to appear according to characteristics of bend flow and its scale is shown in Fig. 1c. The transverse water-surface gradient of the bend flow produces the bend circulation, with flow directing toward the concave bank in the water surface. This provides the initial velocity of levee breach flow. River flow can flow into the land region easily. At the end of the flume, there were two sluice gates and the sluice gate at the river region was used to adjust the water level. Breach erosion was started when the water level surpassed the elevation of the initial breach.

Four automatic water-level gauges were placed at the point numbered from S1 to S4 shown in Fig. 1a. S2 and S4 were in the land region while the others in the river region. A topography meter was placed above the initial breach, measuring the breach profile variation with time by moving back and forth. Velocity changes near the breach were measured by an acoustic Doppler velocimeter (ADV). The location of velocity monitoring points (M_1 and M_2) is shown in Fig. 1b and Fig. 1d. The breach development was recorded by a camera fixed at the flume wall near the breach.

Experiment cases are listed in Table 1. Such main factors as upstream inflow discharge Q, soil porosity e and water content w of the levee materials were considered. The levee was constructed by the lean clay (according to USCS) with grain size distribution shown in Fig. 2. As can be seen, the soil consists of 10% clay particles (d<0.005 mm), 70% silt particles (0.005 mm<d<0.075 mm) and 10% sand particles (d>0.075 mm). The liquid and plastic limit of the soil is 28.6% and 18.1%

respectively, measured by liquid-plastic limit combined method. Other soil parameters such as density ρ, dry density ρ_d, soil cohesion c and initial friction angle φ are all affected by e and w.

The levee was constructed by gradually adding soil and compacting, layer by layer. The soil density was confined to control the levee porosity. Before experiments began，the levee surface in the river region was covered with thin films to prevent infiltration and soil samples were selected from the levee to test w, e, c and φ. The tested values are listed in Table 1. Flow entering the flume was adjusted until the discharge reached the desired value listed in Table 1. After that, the sluice gate at the river region was adjusted to ensure a very slow rise of the water level. The thin films were removed just before the flow overflowed the levee top. Then levee erosion process was started.

3 Levee breaching process

3.1 General description

The process of overtopping breaching can be subdivided into three stages according to the breach erosion characteristics shown in Fig. 3. The initial stage, characterized by flow shear erosion on the levee slope at the land side, is named as slope erosion stage (shown in Fig. 3a). In this stage, there appeared some small scour holes on the land-side slope. Enlargement of the scour holes steepened the slope and then a large-scale scarp known as headcut developed (shown in Fig. 3b). This is the beginning of the second stage defined as headcut retreat stage shown in Fig. 3b, Fig. 3c, Fig. 3d and Fig. 3e. At the end of this stage, the breach cross-section was almost washed out and a deep gully formed (shown in Fig. 3f). Then flow in the gully began to erode the side slopes of the breach, which is the third-stage erosion defined as breach widening stage.

3.2 Slope erosion stage

Initial erosion of this stage usually occurred at the toe of the levee at the land side, due to large flow shear stress there shown in Fig. 4. Fig. 4 shows the water surface and flow shear stress distribution at an instant after overtopping of a levee calculated by Briaud et al. (2008) with a two-dimensional free surface flow model. The large negative shear stress at the toe is caused by flow separation due to sharp corners between the levee and bed surface (Briaud et al., 2008). If the shear stress there surpassed the soil critical shear stress, cohesive soil blocks would be eroded and a scour hole (shown in Fig. 3a) appeared at the originally relatively smooth levee surface. The small scour holes increased bed roughness and flow turbulence, which in turn accelerated the local scour, making the scour hole enlarge. Due to the nonuniformity of the levee body, scour holes may also appear at other weak places but developed more slowly and finally merged into the large scour hole at the bottom.

3.3 Headcut retreat stage

According to the shape of the headcut appearing at this stage, the headcut can be categorized into two basic forms, single-step form (Fig. 5a and Fig. 5d) and multiple-step form (Fig. 5b and Fig. 5c). Initially, an incomplete single-step headcut appeared due to the bottom erosion (shown in Fig. 3b and Fig. 5a). After the headcut retreated to the brink of the levee crest, a multi-step headcut appeared due to the layer construction of the levee (shown in Fig. 3 c, Fig. 3d, Fig. 5b and Fig. 5c) and at last, all the steps disappeared and there appeared a complete single-step headcut (shown in Fig. 3e and Fig. 5d).

When the overflow velocity was small, the flow just streamed down along the vertical headcut surface where flow shear erosion mainly occurred.

If the flow velocity increased, the overflow departs from the headcut surface, forming an impinging jet. For multi-step headcut, when the flow velocity was not large enough, there may exist multiple small impinging jets due to the steps (shown in Fig. 3d and Fig. 5c). For single-step headcut or multiple-step headcut with large-velocity overflow, there existed a single impinging jet (shown in Fig. 3b, Fig. 3e, Fig. 5a, Fig. 5b and Fig. 5d). The single jet and small bottom jet directly impinged the non-erodible foundation, with part reflected toward the headcut as a reverse roller which undermined the headcut bottom. The other small upper jets, however, impinged the erodible platforms of the headcut steps, exerting both normal and horizontal shear stress on the platforms. The platforms were eroded or collapsed and finally disappeared. The above erosion mode caused by impinging jets, was defined as jet impinging erosion.

It should be noted that in this stage flow shear erosion and jet impinging erosion usually appeared in company with each other. The common combination style is that flow shear erosion happened above and the other happened below. Or they distributed alternatively along the river flow direction. Except for the two erosion modes, discrete mass failure may also appear during the erosion process. The headcut retreated gradually by the above three soil destruction modes.

It can be discovered that the headcut height reduction, which was caused by flow shear erosion on the breach top, was much slower than the headcut backward migration. This made the overflow velocity quite small (about 0.2 m/s), hardly influenced by inflow discharge. So when soil properties were similar and the inflow discharge the same (Case 3 and Case 4, for example), headcut retreat rate was almost the same (shown in Fig. 6).

Furthermore, there exists a positive correlation between headcut retreat rate and soil water content while negative when it comes to soil porosity. For example, headcut of Case 2 with a larger soil porosity, retreat three times faster than that of Case 1 (shown in Fig. 6). And for Case 1 with higher soil water content, it costs much more time for headcut retreat process compared with Case 3 (shown in Fig. 6). A reasonable explanation for this phenomenon is that small soil porosity or large soil water

content can result in large soil cohesion as shown in Table 1. While for cohesive soil, large cohesion between particles can enhance soil erosion resistance decisively.

3.4 Breach widening stage

During the breach widening stage, the side slopes of the breach under water were eroded by flow shear stress and retreated, rendering the remaining part above the water suspending as cantilever shown in Fig. 3f.

The breach widening process is shown in Fig. 7. It can be seen that initially, the migration rate of the upstream and downstream side slope of the breach was similar. But afterwards, the downstream side was eroded faster. This can be explained by the flow structures shown in Fig. 3f. The breaching main flow concentrates near the downstream side slope and eroded its toe. Fig.8 shows the calculated flow field near the breach of Case 2 when the breach width is about 40 cm using the following 2D depth-averaged numerical model. The flow velocity near the downstream side is larger than that near the upstream side. Meanwhile, around the downstream side, the flow velocity near the toe of the land region is larger than that of the river region. The flow structure corresponds well with the final breach form shown in Fig. 9.

The migration rate of the side slopes was influenced by both the levee erosion resistance and nearby flow structures. In this period, when soil properties were the same, larger upstream discharge of Case 4 resulted in larger flow velocity near the breach and consequently a faster side slope retreat rate compared to Case 3. The same as headcut retreat rate, decrease of levee soil porosity and increase of soil water content can both accelerate breach widening.

The cantilever above the water surface can sustain itself for a while before collapse attributed to inner tensile stress of soil. Assuming that the cantilever is cuboid and sustains flexural deformation, then the forces acting on the cantilever in critical fracture state is shown in Fig. 10. In such state, the inner tensile stress on top of the fracture surface reaches the soil tensile strength σ_t and the moment equilibrium equation of the cantilever per unit width is expressed as (Fukuoka, 1994)

$$\frac{1}{2}GL_c = \frac{1}{6}\sigma_t H_c^2 \tag{1}$$

where G is the weight of the cantilever per unit width expressed as $G = \gamma L_c H_c$; γ is the unit weight of the cantilever expressed as $\gamma = \rho g$. L_c and H_c are the length and height of the cantilever when fracturing, respectively.

The critical cantilever length can be deduced from Eq. (1) as:

$$L_c = \sqrt{\sigma_t H_c / 3\gamma} \tag{2}$$

Assuming that the soil tensile strength is 0.7 times of soil cohesion (Zhu, 2008), then the average critical cantilever length L_c can be calculated by Eq. (2) and the results are shown in Table 2. It can be seen that the calculated L_c rather approximates to the measured value, which proves the reasonability of the above assumption about the cantilever fracture.

4 Flow characteristics near the breach

4.1 Flow velocity and water level variation

The velocity monitoring point of Case 1 is located at M_1 while that of Case 2 is located at M_2 shown in Fig. 11. Fig. 12 shows variation with time of the water level at monitoring point S2 *Z* (representing the flooding routine process of the land region) and the water surface velocity near the breach at monitoring point M_1 (M_2). Directions of the velocity are shown in Fig. 11. Direction x' is horizontal and perpendicular to the levee axis pointing to the land region, direction y' is horizontal and parallel to the levee axis pointing to the downstream while direction z' is vertically upward. Ux'、Uy' and Uz' are respectively velocity in the x', y' and z' direction. *U* is the resultant velocity.

It can be seen that the variation of water level in the land region corresponded well with the breach height *H*, increasing gradually initially but sharply later along with a sharp drop of breach height. Then it kept almost constant, although the breach went on widening.

The variation of the resultant flow velocity was also related to the breach height changes. For Case 1 (shown in Fig. 12a), before 75 min, *U* increased slowly with gradual decrease of the breach height. From the time of 75 min, the breach height *H* began to drop sharply and correspondingly, *U* began to raise sharply with 1 minute lag. At the time of 78 min, *H* reduced to the minimum value of zero and the flow velocity *U* reached the maximum value of 0.7 m/s. After that, along with the increasing water level in the land region, *U* dropped gradually and stabilized itself at the value of about 0.5 m/s.

General flow direction and its variation trend can be deduced from the magnitude of the component flow velocities. Initially, Uz' was almost zero, demonstrating the two-dimensional characteristics of the flow. Ux' was almost the same with Uy' initially but surpassed it afterwards, indicating that flow was toward the breach due to the decrease of the breach height. With the sharp decrease of the breach height, there appeared different variation trend of Uy' for Case 1 and Case 2. For Case 1 (shown in Fig. 12a), M_1 is located at the upstream side of the breach and it is inevitable that there exist component velocity toward downstream direction so Uy' increased and kept at a relatively larger value. While for Case 2 (shown in Fig. 12b), M_2 is located in the middle of the breach, flow velocity there was directly toward the land region so Uy' decreased to almost zero.

4.2 Overflow rates

It is rather hard to acquire the flow rates over the levee breach directly by measurements. So a depth-averaged 2-D flow model was established to compute them. In the calculating process, the breach geometry was modified at each time step according to the above measured headcut retreat and breach widening process.

4.2.1 Numerical methods

The governing equations, written as vector form, are given as follows:

$$\frac{\partial \boldsymbol{U}}{\partial t}+\frac{\partial \boldsymbol{F}}{\partial x}+\frac{\partial \boldsymbol{G}}{\partial y}=\boldsymbol{S} \tag{3}$$

where ***U, F***, ***G*** and ***S*** are expressed as

$$\boldsymbol{U}=\begin{bmatrix} h \\ hu \\ hv \end{bmatrix},\quad \boldsymbol{F}=\begin{bmatrix} hu \\ hu^2+gh^2/2 \\ huv \end{bmatrix},\quad \boldsymbol{G}=\begin{bmatrix} hv \\ huv \\ hv^2+gh^2/2 \end{bmatrix},\quad \boldsymbol{S}=\begin{bmatrix} 0 \\ gh(S_{bx}-S_{fx}) \\ gh(S_{by}-S_{fy}) \end{bmatrix} \tag{4}$$

where x, y are Cartesian coordinates shown in Fig. 13a; h is water depth, u, v are flow velocity in the x and y direction, respectively. S_{bx}, S_{by}, S_{fx} and S_{fy} are respectively bed slope and friction slope in the x and y directions. S_{fx} and S_{fy} are expressed by Manning equation as follows

$$S_{fx}=\frac{n^2u\sqrt{u^2+v^2}}{h^{4/3}},\qquad S_{fy}=\frac{n^2v\sqrt{u^2+v^2}}{h^{4/3}} \tag{5}$$

where n is Manning roughness coefficient.

Equation (3) was discretized by finite volume method in space. The calculating grids are shown in Fig. 13b. At any calculating cell (i, j), the equation was discretized as

$$\frac{\mathrm{d}\boldsymbol{U}_{i,j}}{\mathrm{d}t}=-\frac{1}{\Delta x}\left(\boldsymbol{F}_{i+\frac{1}{2},j}-\boldsymbol{F}_{i-\frac{1}{2},j}\right)-\frac{1}{\Delta y}\left(\boldsymbol{G}_{i,j+\frac{1}{2}}-\boldsymbol{G}_{i,j-\frac{1}{2}}\right)+\boldsymbol{S}_{i,j} \tag{6}$$

where Δx and Δy are respectively grid size in the x and y direction. The numerical fluxes ***F*** and ***G*** were calculated by WENO–Roe method based on Riemman solvers that can capture flow discontinuity (Dou et al., 2014). Third-order Runge–Kutta method was used to discretize Eq. (6).

As the schemes are based on explicit algorithms, time step should satisfy Courant-Friedrichs-Lewy (CFL) criteria (Toro, 1999):

$$N_{cfl} = \Delta t \times \min\left(\frac{|u|+\sqrt{gh}}{\Delta x}, \frac{|v|+\sqrt{gh}}{\Delta y}\right) \le 1 \tag{7}$$

where N_{cfl} is Courant number; Δt is computational time step; N_{cfl} was valued much smaller than unity because of large bed elevation variation involved in calculation of levee break flow. Here, it was proved that the value of 0.03 for N_{cfl} can achieve reasonable result.

Rectangular grids with size set as 0.5 cm×0.5 cm were deployed. To avoid zigzag boundary caused by rectangular grids, the calculating area was extended to a large rectangle *ABCD* shown in Fig. 13a. Elevations of the area outside the flume were all assigned a larger value than the maximum water level in the flume. A simplified balancing-point method (Zhou, 1988) was used to simulate boundary conditions. The method is described in detail as follows. In the *x* direction, for example, it is assumed that the node numbered (i, j) is outside the flume wall while the node i+1 is inside with water depth h_{i+1}, flow velocity u_{i+1} and v_{i+1}. Then the variables at the node (i, j) are assigned h_{i+1}, $-u_{i+1}$ and v_{i+1} respectively. This is on the assumption that boundary node is in the middle of the two nodes and the boundary is vertical to the *x* direction at the point. When grid size is sufficiently small, the method is viable, without changing the real boundary obviously.

During the propagation process of levee breach flow on riverbed, there may exist temporary dry nodes without water. To handle the problems, a minimum water depth of 0.001 m was defined and initially all dry nodes were set as the minimum water depth. At a given simulation time, if water depth at a node was less than the minimum water depth, then the node is regarded dry and velocity was set as zero.

The flow rates at the inflow boundary *CE* were set as that listed in Table 1 for each case, and the measured water level process at the point S4 was set as outflow boundary condition. Before overflow calculation, a steady-state flow condition in the river region was calculated by given inflow rate in Table 1 and corresponding water level at the point S3. The steady-state flow condition was set as initial condition of overflow. The value of Manning roughness coefficient (0.02) was acquired by comparing calculated and measured water level.

The model has been verified by Dou et al. (2014).

The flow parameters for calculating the overflow rates were defined at the initial land-side brink of the levee top. According to the computed velocity and water depth at each grid between the breach, average velocity and water depth at the brink can be acquired, by which the breaching overflow rates were calculated.

4.2.2 Calculated results and analysis

The calculated overflow rates Q_b are shown in Fig. 14. Initially, the overflow rate was very small and increased gradually due to the large and slowly-reducing breach height. Then it increased sharply, with a rapid decrease of breach height. Just after the breach height decreased to zero, the overflow rate reached its maximum value and then decreased. Finally, the overflow rate kept almost stable at a certain value. It can be also seen that the maximum overflow rate for Case 4, with a larger inflow discharge (28.53 L/s) than the other three (14.64 L/s), is also larger.

To verify the reasonability of the modelled results, we take use of the measured velocity of Case 2. For Case 2, the velocity monitoring point is located at the middle of the breach and the flow direction there was directly toward the land region. And the measured velocity here can represent the average breaching flow velocity. In Table 3, we list the breach geometry parameters (the breach width B and the breach height H), the hydraulic parameters (the water head above the breach crest h' and the measured velocity U), the estimated breach discharge Q_{bm} (calculated by $Q_{bm} = Bh'U$) and the numerically calculated breach discharge Q_b. It can be seen that the numerically calculated breach discharge matches well with the estimated values overall.

The breach overflow rates can also be simulated by broad-crested weir flow formula, which can be expressed as (Hager and Schwalt, 1994)

$$Q_b = C_d \sqrt{2g} B h_0^{1.5} \tag{8}$$

where B is the levee breach width and h_0 is approaching energy head. $h_0 = h' + v_a^2 / 2g$, with v_a the approaching velocity and h' the water head above the breach crest. C_d is dimensionless discharge coefficient, the value of which depends on the breach shape. When the effect of approaching velocity can be omitted, Eq. (8) can be expressed as

$$Q_b = C_d \sqrt{2g} B h'^{1.5} \tag{9}$$

For the simplicity of analysis, Q_b, B and h are nondimensionalized by gravity acceleration g and the initial breach height H_0 to Q_{b*}, B_* and h_* respectively (Coleman et al., 2004). $Q_{b*} = Q_b / g^{0.5} H^{2.5}$; $B_* = B / H$; $h_* = h / H$. Then Eq. (9) can be replaced by

$$Q_{b*} = \sqrt{2} C_d B_* h_*^{1.5} \tag{10}$$

Depending on the simulated overflow rates and measured breach hydraulic parameters, the relation between Q_{b*} and $B_* h_*^{1.5}$ is shown in Fig. 15. With a correlation coefficient of 0.93, the fitting relation of Q_{b*} and $B_* h_*^{1.5}$ can be expressed as

$$Q_{b*} = 0.34 B_* h_*^{1.5} \tag{11}$$

From Eq. (10) and Eq. (11), C_d is deduced as 0.24, smaller than the discharge coefficient of common rectangular weirs (Hager and Schwalt, 1994). This may result from both the initial trapezoid shape of the breach cross-section and the large surface roughness appeared later at the land side (Pařílková et al., 2012).

At the later stage of the headcut retreat, the overflow rate of Case 4 is much larger than that of the other three cases with the same B and $h^{'}$. This may result from larger approaching velocity caused by larger inflow discharge.

5 Discussion

The main factor resisting flow erosion of non-cohesive soils is the effective gravity of sediment particles. While for compacted cohesive soils, the main factor is the cohesive force between soil particles, which is usually much larger than the effective gravity of non-cohesive sediment particles. This make the affecting factors for overtopping breaching of non-cohesive and cohesive levees quite different. Non-cohesive levee breaching rate is mainly affected by the particle diameter (it is consumed the sediments are with the density). While for cohesive levee breach, the main factors are those affect the cohesive force such as soil composition, compaction degree and soil water content. And the breaching processes of the two kinds of levees are quite different because of the different resisting force. Compared with non-cohesive levees, the overtopping breaching of cohesive levees are much slower and it consists two special stage-the slope erosion stage and headcut retreat stage. This can be attributed to the strong anti erodibility of cohesive soils. The cohesive levee crest and land-side levee slope are eroded with slower rate and hardly form erosion gully, thus the slope erosion stage exists for a period. And because the erosion rate of the levee crest is smaller and the land-side levee slope are hard to collapse, the morphology of headcut forms. For non-cohesive levees, the fast-eroded sediment materials from the levee crest deposit at the land-side levee slope toe and frequent collapse in the land-side slope occurs. This makes the breach a gentler slope and seldom form abrupt elevation changes like headcut.

6 Conclusions

Overtopping breaching of levees constructed with cohesive soils can be subdivided into three stages according to breach erosion characteristics. The initial stage was defined as slope erosion stage, characterized by flow shear erosion on land-side slope and small scour hole at bank toe. The next stage was headcut retreat stage, in which single-step form and multi-step form headcut can be discovered. Both flow shear erosion and jet impinging erosion existed in this stage. Headcut migration rate was hardly influenced by inflow discharge but had more to do with soil properties. Increase of soil water content or decrease of soil

porosity can both decrease headcut migration rate. The final stage was breach widening stage, including erosion of side slopes under water and the cantilever collapse above water surface. The migration rate of side slopes was affected by both soil erosion resistance and nearby flow characteristics. The maximum cantilever length, however, was influenced by soil density, average cantilever height and soil tensile strength.

Both the water level and flow velocity variation near the breach corresponded well with the breach height changes. The magnitude of the component flow velocities near the breach can indicate general direction of the breaching flow. Along with the decrease of the breach height, the breaching flow began to be toward the breach. And near the breach, flow direction at upstream point was more toward the downstream while flow direction of downstream point was directly toward the land region.

The calculated overflow rates variation trend was the same with that of flow velocity near the breach and the overflow rate increased along with the inflow discharge. By substituting the calculated overflow rates and measured breach size into the broad-crested weir flow formula, the discharge coefficient was deduced, which was smaller than that of common rectangular broad-crested weirs.

Acknowledgements. The work was supported by Natural Science Foundation of China [grant 11502174], [grant 11272240] and the Fundamental Research Funds for the Central Universities of China [grant 2042015kf0047].

References

Briaud, J. L., Chen, H. C., Govindasamy, A. V., and Storesund, R.: Levee erosion by overtopping in New Orleans during the Katrina Hurricane, J. Geotech. Geoenviron., 134, 618-632, 2008.

Coleman, S. E., Andrews, D. P., and Webby, M. G.: Overtopping breaching of noncohesive homogeneous embankments, J. Hydraul. Eng., ASCE, 128, 829-838, 2002.

Dou, S. T., Wang, D. W., Yu, M. H., and Liang, Y. J.: Numerical modeling of the lateral widening of levee breach by overtopping in a flume with 180° bend, Nat. Hazards Earth Syst. Sci., 14, 11-20, 2014.

Fukuoka, S.: Erosion processes of natural river bank, in: Proceedings of the 1st International Symposium on Hydraulic Measurement, Beijing, China, 223-229, 1994.

Hager, W. H., and Schwalt, M.: Broad-crested weir, J. Irrig. Drain. E., ASCE, 120, 13-26, 1994.

Hahn W., Hanson G. J., and Cook K. R.: Breach morphology observations of embankment overtopping tests, in: Proceedings of 2000 Joint Conference on Water Resources Engineering and Water Resources Planning and Management, Minneapolis, USA, 1-10, 2000 (CD-ROM).

Hanson, G. J., Robinson, K. M., and Cook, K. R.: Prediction of headcut migration using a deterministic approach, T. ASAE, 44, 525-531, 2001.

Hanson, G. J., Temple, D. M., and Cook, K. R.: Dam overtopping resistance and breach processes research, in: Proceedings of Association of State Dam Safety Officials Annual Conference 1999, St. Louis, Missouri, USA, 1999 (CD-ROM).

Kakinuma, T., and Shimizu, Y.: Large-scale experiment and numerical modeling of a riverine levee breach, J. Hydraul. Eng., ASCE, 140, 4014039-1-4014039-9, 2014.

Liang, L., Ni, J. R, Borthwick, A. G. L., and Rogers, B.D: Simulation of dike-break processes in the Yellow River. Sci. China. Ser. E., 45: 606-619, 2002.

Morris, M. W., Hassan, M., and Vaskinn, K.: The IMPACT WP2 Technical Reports IV: summary of breach formation field and laboratory data. Available at: http://www.impact-project.net/wp2_technical.htm, 2005.

Osman, A. M., and Thorne, C. R.: Riverbank stability analysis. I: Theory. J. Hydraul. Eng., ASCE, 114, 134-150, 1998.

Pařílková, J., Říha, J., and Zachoval, Z.: The influence of roughness on the discharge coefficient of a broad-crested weir. J. Hydrol. Hydromech., 60, 101-114, 2012.

Pickert, G., Weitbrecht, V., and Bieberstein. A.: Breaching of overtopped river embankments controlled by apparent cohesion. J. Hydraul. Res., 49, 143-156, 2011.

Pontillo, M., Schmocker, L., Greco, M., and Hager, W. H.: 1D numerical evaluation of dike erosion due to overtopping. J. Hydraul. Res., 48, 573-582, 2010.

Powledge, G.R., Ralston, D.C., Miller, P., Chen, Y.H., Clopper, P.E., and Temple, D.M.: Mechanics of overflow erosion on embankments II: hydraulic and design considerations, J. Hydraul. Eng., ASCE, 115, 1056-1075, 1989.

Ralston, D.C.: Mechanics of embankment erosion during overflow, in: Proceedings of 1987 ASCE National Conference on Hydraulic Engineering, Williamsburg, Virginia, USA, 733-738, 1987.

Schmocker, L. and Hager, W. H.: Modelling dike breaching due to overtopping. J. Hydraul. Res., 47, 585-597, 2009.

Schmocker, L. and Hager, W. H.: Plane dike-breach due to overtopping: effects of sediment, dike height and discharge. J. Hydraul. Res., 50, 576-586, 2012.

Stein, O. R. and LaTray, D. A.: Experiments and modeling of head cut migration in stratified soils. Water. Resour. Res., 38, 1284, doi: 10.1029 /2001WR001166, 2002.

Toro, E. F.: Riemann solvers and numerical methods for fluid dynamics: 2nd edition, Springer, Berlin, 1999.

Wahl, T. L.: Uncertainty of predictions of embankment dam breach parameters, J. Hydraul. Eng., ASCE, 130, 389-397, 2004.

Yu, M. H., Wei, H. Y., Liang, Y. J., and Zhao, Y.: Investigation of Non-cohesive Levee Breach by Overtopping Flow, J. Hydrodyn., 25, 542-579, 2013.

Zhang, J. Y., Li, Y., Xuan, G. X., Wang, X. G., and Li, J.: Overtopping breaching of cohesive homogeneous earth dam with different cohesive strength. Sci. China. Ser. E., 52, 3024-3029, 2009.

Zhao, G., Visser, P. J., Peeters, P., and Vrijling, J. K: Headcut migration prediction of the cohesive embankment breach, Eng. Geol., 164, 18–25, 2013.

Zhou, J. J.: A balancing-point method for simulating boundary conditions in rectangular grids. Journal of Hydraulic Engineering, 7, 14-18, 1988. (in Chinese)

Zhu, C. H., Liu, J. M., Yan, B. W., and Ju, J. L: Experimental study on relationship between tensile and shear strength of unsaturation clay earth material. Chinese Journal of Rock Mechanics and Engineering, 27, 3453-3458, 2008. (in Chinese)

Zhu, Y. H.: Breach growth in clay-dikes, Ph.D. thesis, Delft University of Technology, Delft, the Netherlands, 231 pp., 2006.

Zhu, Y. H., Visser, P. J., Vrijling, J. K., and Wang, G. Q: Experimental investigation on breaching of embankments. Sci. China. Ser. E., 54: 148-155, 2011.

Table 1 Experiment cases and parameters

Case	Q (L/s)	w (%)	e (%)	ρ (kg/m^3)	ρ_d (kg/m^3)	c (KPa)	φ (°)
1	14.64	21.2	41.2	1920	1590	22.22	25.79
2	14.64	21.07	42.88	1870	1540	21.85	25.13
3	14.64	19.8	40.8	1910	1600	20.94	25.77
4	28.53	19.9	40.8	1920	1600	21.07	26.4

Table 2 Calculated critical cantilever length

Case	ρ (kg/m^3)	Average H_C (cm)	c (KPa)	σ_t (KPa)	Calculated L_C (cm)	Measured L_C (cm)
1	1920	4.7	22.22	15.554	11.4	11.1
2	1870	4.4	21.85	15.295	9.9	8.9
3	1910	4.4	20.94	14.658	9.4	7.8
4	1920	4.5	21.07	14.749	9.8	8.1

Table 3 Numerically calculated breach discharge and estimated values

t (min)	H (cm)	B (cm)	h' (cm)	U (m/s)	Q_{bm} (L/s)	Q_b (L/s)
10	15.7	20	1.8	0.193	0.695	0.655
17	15.5	20	2	0.198	0.792	0.964
19	15	20	2.5	0.207	1.035	1.416
21	13	20	4.5	0.324	2.916	1.922
22	5	20	12.5	0.499	12.475	11.601
23	0	20	16.9	0.579	19.57	18.744
25	0	36	13.3	0.407	19.487	18.292
28	0	43	13	0.318	17.776	15.551

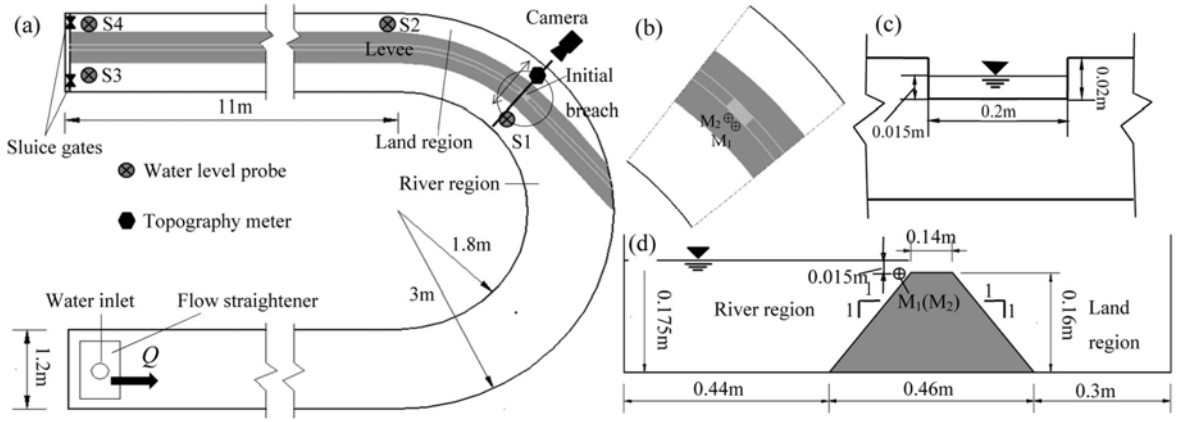

Figure 1 Levee model: (a) Top view of experiment layout, (b) Velocity monitoring point, (c) Longitudinal section of initial breach and (d) Transverse section of initial breach

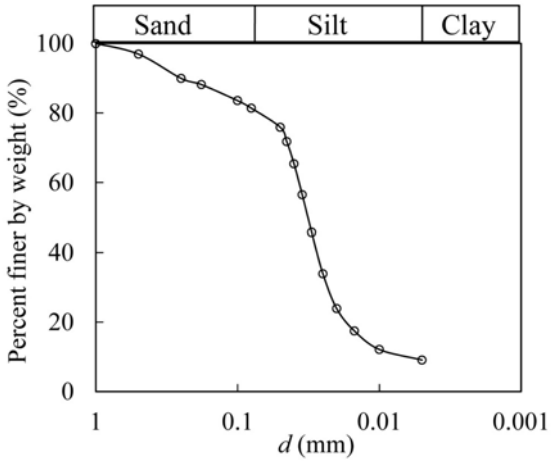

Figure 2 Grain size distribution of experiment materials

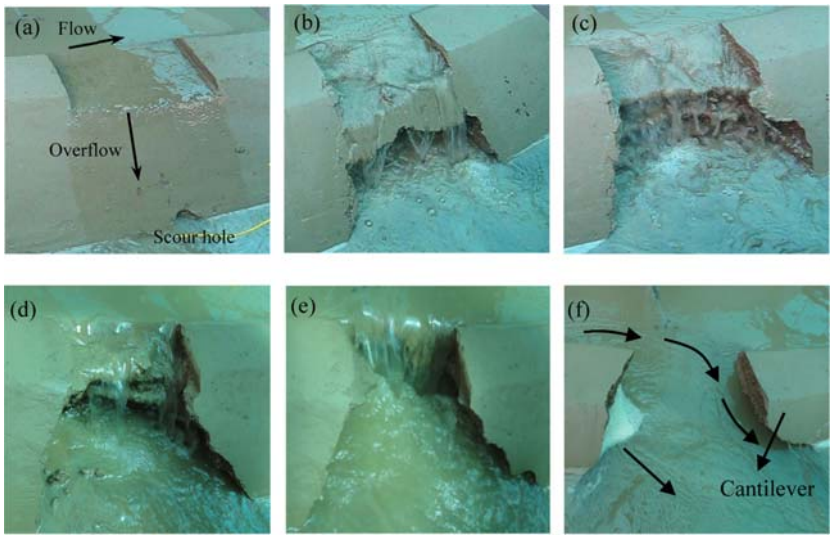

Figure 3 Levee breaching process: (a) Slope erosion stage; (b), (c), (d) and (e) Headcut retreat stage; (f) Breach widening stage

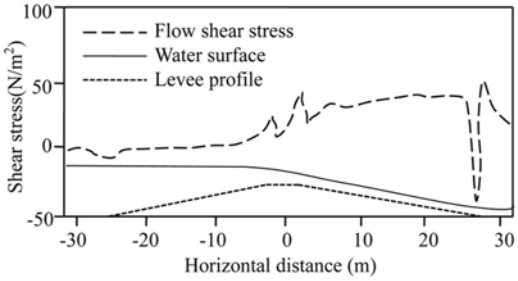

Figure 4 A typical flow shear stress distribution along the dike calculated by Briaud et al. (2008)

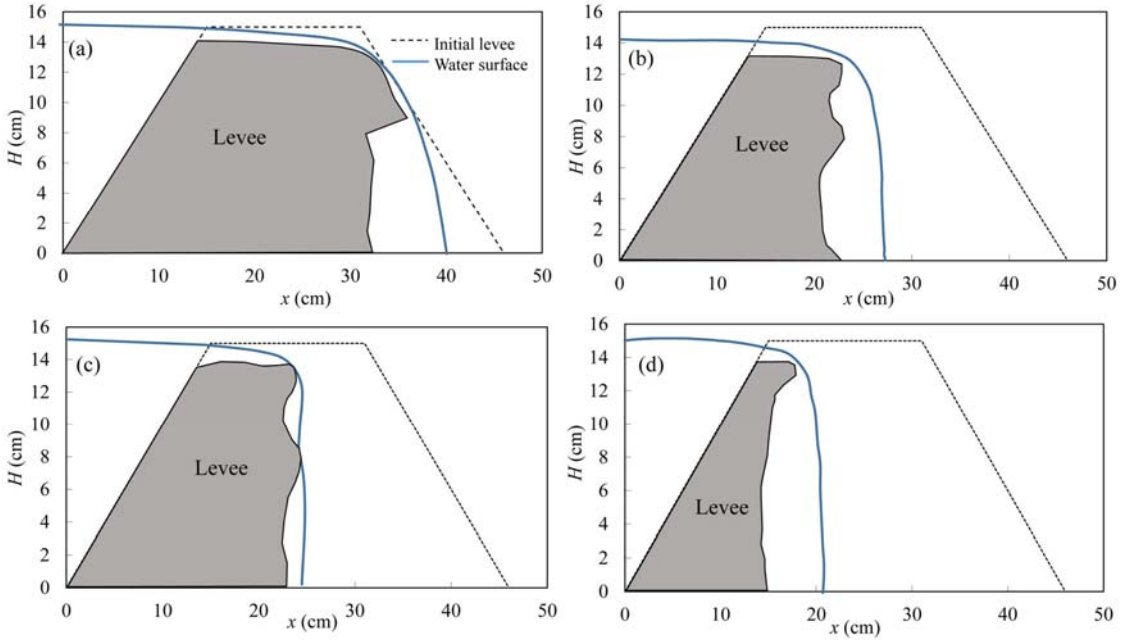

Figure 5 Headcut type: (a) Single headcut with single jet; (b) Multiple-step headcut with single jet; (c) Multiple-step headcut with multiple jets; (d) Single headcut with single jet

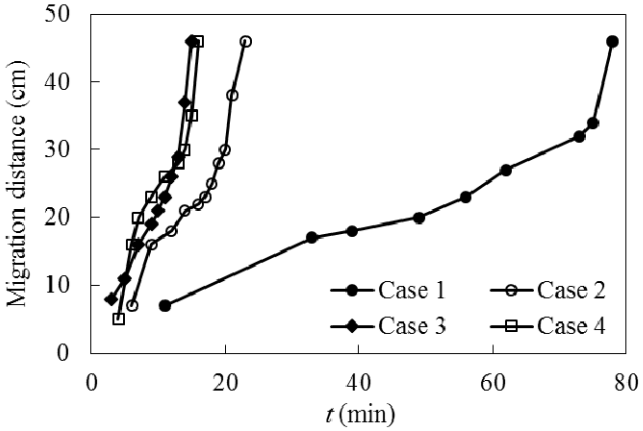

425

Figure 6 Headcut retreat process

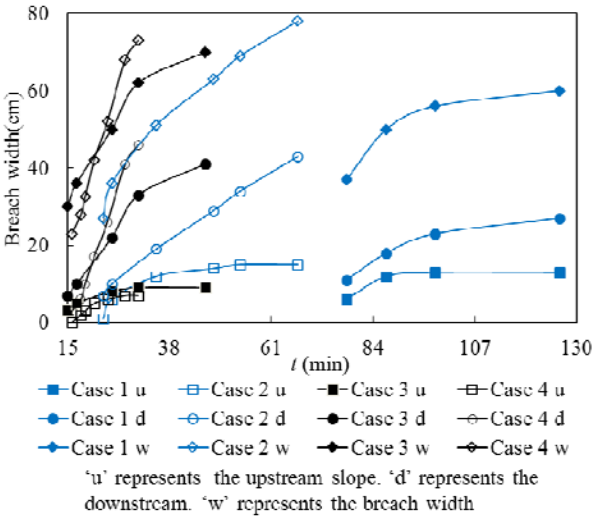

Figure 7 Breach widening process

430

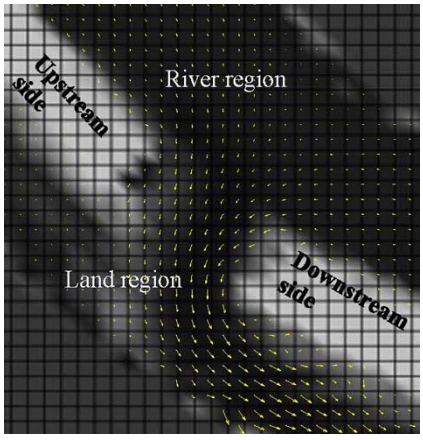

Figure 8 Flow field of Case 2 (B=40cm)

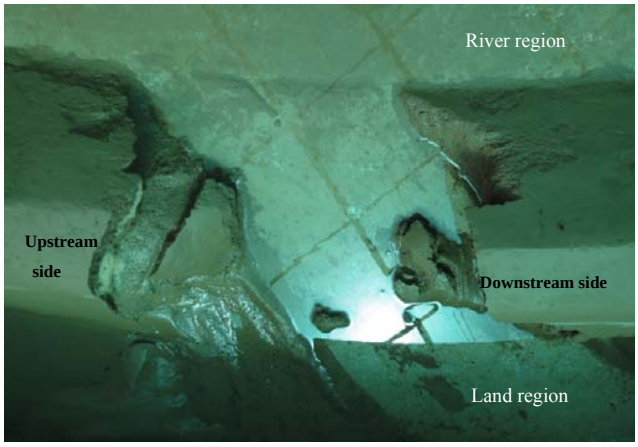

Figure 9 Final breach form

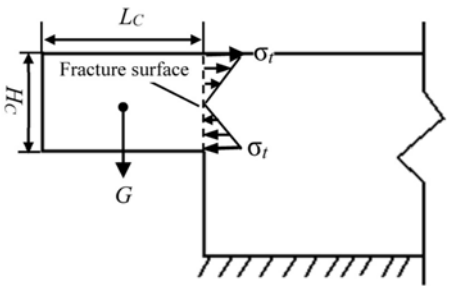

Figure 10 Critical fracture state of a cantilever

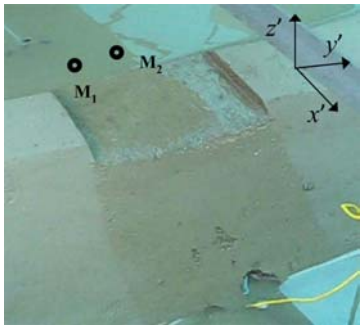

Figure 11 Velocity monitoring point

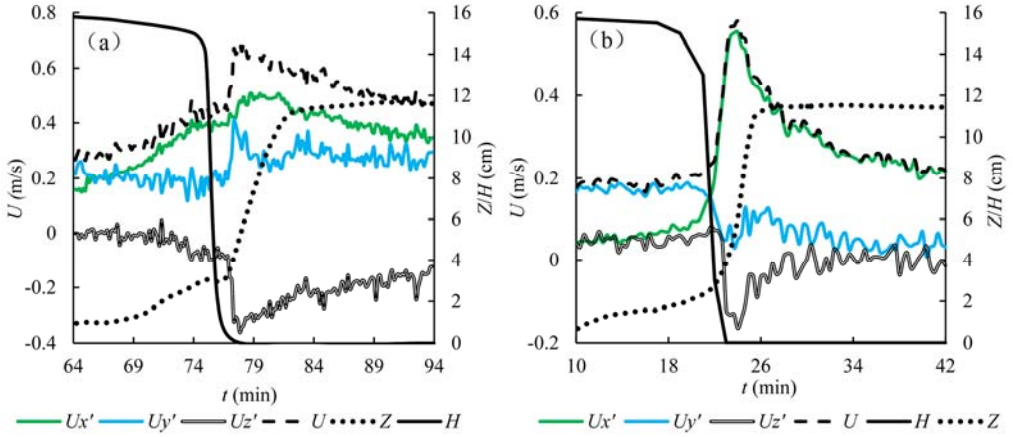

445 Figure 12 Relation between water level, velocity and breach height: (a) Case C-1, (b) Case C-2

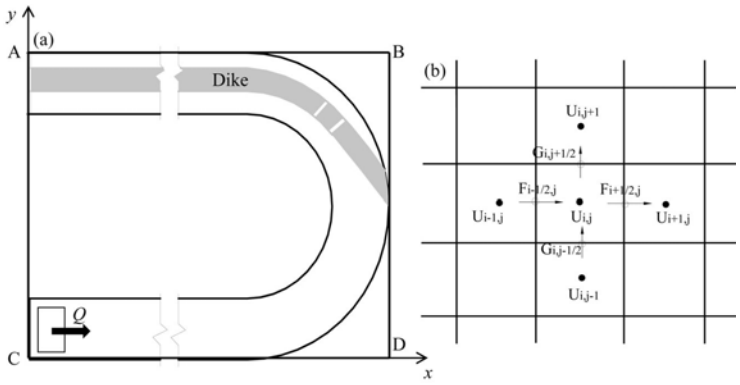

Figure 13 Calculated area

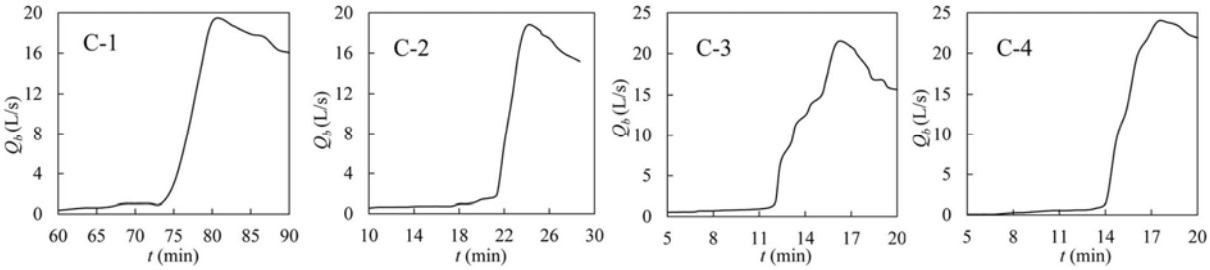

450 Figure 14 Simulated overflow rates

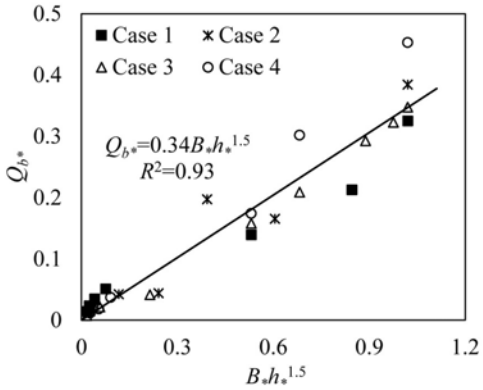

Figure 15 Fitting relation of Q_{b*} and $B_*h_*^{1.5}$

455